

# Highly Conductive Off-Stoichiometric Zirconium Oxide Nanofibers with Controllable Crystalline Structures and Bandgaps and Improved Electrochemical Activities

Na-Won Lee,<sup>†</sup> Ki Ro Yoon,<sup>‡</sup> Jae-Yun Lee,<sup>†</sup> Yoonsu Park,<sup>§</sup> Seong-Ji Pyo,<sup>†</sup> Ga-Yoon Kim,<sup>†</sup> Don-Hyung Ha,<sup>§</sup> and Won-Hee Ryu<sup>\*,†</sup>

<sup>†</sup>Department of Chemical and Biological Engineering, Sookmyung Women's University, 100 Cheongpa-ro 47-gil, Yongsan-gu, Seoul 04310, Republic of Korea

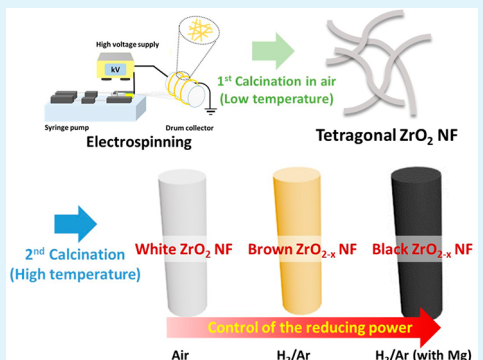
<sup>‡</sup>Technical Textile and Materials R&BD Group, Korea Institute of Industrial Technology (KITECH) 143, Hangga-ro, Sangnok-gu, Ansan-si, Gyeonggi-do 15588, Republic of Korea

<sup>§</sup>School of Integrative Engineering, Chung-Ang University, 84 Heukseokno, Dongjak-gu, Seoul 06974, Republic of Korea

## Supporting Information

**ABSTRACT:** The structural and morphological control of durable valve metal oxides with bandgaps over 5 eV (e.g.,  $ZrO_2$ ) paves the way for the development of bifunctional electrochemical energy devices with both good stabilities and electronic conductivities. Herein, a tailored synthesis of highly conductive off-stoichiometric  $ZrO_{2-x}$  nanofiber materials under a controlled reducing atmosphere is reported. The bandgap and corresponding charge conductivity of  $ZrO_{2-x}$  are simultaneously tuned (in the range of visible colors (white, brown, and black)) by generating reduced  $Zr^{3+}$  and oxygen vacancies. The morphological and structural evolution of the  $ZrO_{2-x}$  nanofibers obtained under different reducing atmospheres are investigated in detail. Electrochemical kinetics in aqueous and nonaqueous media are promoted by employing a darker  $ZrO_{2-x}$  nanofiber electrode. The functionalizing valve metal oxides with a facile charge transfer inspire an advanced design for future electrochemical and electronic devices.

**KEYWORDS:** *electrospinning, nanofiber, zirconium oxide, valve metal oxide, oxygen deficiency*



## INTRODUCTION

Forthcoming technologies for the development of advanced electronic and energy devices should be focused on functional and durable electrode materials based on earth-abundant elements.<sup>1–3</sup> Valve metal oxides frequently used in diverse industries have been defined as a family of chemically and mechanically stable oxide materials including valve transition metals (e.g., Ti, Zr, Hf, W, and Mo) with exceptionally high bandgaps in the range of 3.0–7.0 eV.<sup>4,5</sup> Among them, zirconium oxide ( $ZrO_2$ ) (referred to as zirconia) has exceptional structural and mechanical stabilities, leading to high melting and boiling temperatures (2,715 and 4,300 °C, respectively) and negligible solubility against a corrosive environment.<sup>6</sup> In this regard,  $ZrO_2$  materials have been intensively employed in various applications such as insulating and protecting agents, refractory material components, highly durable devices, solid electrolytes, and biocompatible applications (e.g., implant and artificial bone).<sup>7</sup> However,  $ZrO_2$  has rarely been considered an “electrode material” or “electrical substrate” candidate owing to its high bandgap (over 5 eV) as an insulator according to the trade-off relationship between the robust stability and electronic conductivity.<sup>8</sup> Preferred

electrode materials should simultaneously involve (i) fast electron transport pathways when used as electronic substrates, (ii) enhanced functionality for high-performance devices, (iii) robust stability against a severe operating environment, and (iv) long lifetime.

The fine synthetic control of valve metal oxides can be used to modulate their intrinsic properties including electronic, optical, and catalytic characteristics.<sup>9–11</sup> For example, oxygen-deficient  $TiO_{2-x}$  materials, referred to as black  $TiO_{2-x}$ , can be easily obtained by a thermal treatment under a reducing atmosphere.<sup>12,13</sup> The reducing treatment of  $TiO_2$  generates reduced  $Ti^{3+}$  ions and oxygen vacancies to satisfy the charge neutrality, thereby achieving a significantly decreased bandgap by ~2.0 eV and improved charge (electron, ion) conductivities on the surface.<sup>14,15</sup> The black color implies that the  $TiO_{2-x}$  materials fully absorb light including the whole visible-light range owing to the reduced bandgap.<sup>13</sup> Over the past few years, modified  $TiO_{2-x}$  electrodes have facilitated electro-

Received: February 10, 2019

Accepted: April 23, 2019

Published: April 23, 2019

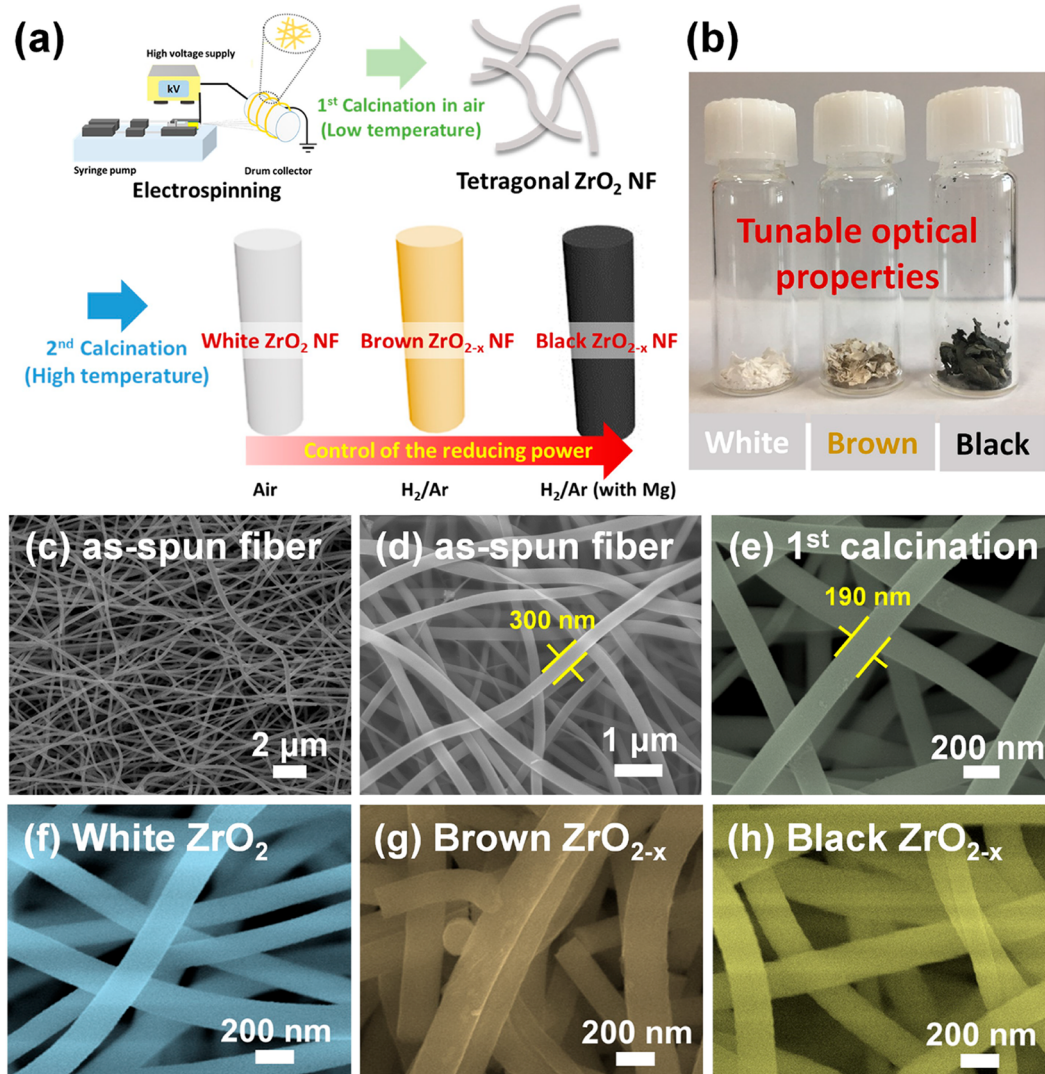


**Figure 1.** (a) Schematic illustration of the controllable synthetic steps for white, brown, and black  $\text{ZrO}_{2-x}$  NFs under different reducing powers. (b) Tunable optical properties and color changes among the white, brown, and black  $\text{ZrO}_{2-x}$  NFs. (c, d) SEM images of the as-spun composite NFs of Zr precursor with the PVP polymer prepared by electrospinning, acquired at different magnifications. (e) SEM image of  $\text{ZrO}_2$  NFs calcined at 350 °C for 1 h in air (after the first calcination). SEM images of the (f) white  $\text{ZrO}_2$ , (g) brown  $\text{ZrO}_{2-x}$  and (h) black  $\text{ZrO}_{2-x}$  NFs obtained after the second calcination under different reducing atmospheres.

chemical and catalytic reactions (e.g., in batteries, photocatalytic hydrogen generation, environmental pollution removal, and solar cells).<sup>13,16</sup> Inspired from this approach, other “white” valve metal oxides including  $\text{ZrO}_2$  can be transformed to highly conductive “black”  $\text{ZrO}_{2-x}$  oxides by controlling the oxidation number, from  $\text{Zr}^{4+}$  to  $\text{Zr}^{3+}$ , followed by formation of oxygen vacancies. A few studies regarding the artificial synthesis of black  $\text{ZrO}_{2-x}$  for photosensitive applications have been reported.<sup>11,17</sup> However, tailored control of the  $\text{ZrO}_{2-x}$  bandgap for applications to electrode materials has not been yet studied. In addition, a synergistic introduction of nanoscale morphology for an oxygen-deficient  $\text{ZrO}_{2-x}$  structure enables maximization of the surface area proportional to the number of reaction sites. The oxygen defects on the  $\text{ZrO}_{2-x}$  structure can provide improved ionic conductivity in the structure and effective adsorption sites of reactants for catalytic reactions such as oxygen reduction and evolution for electrochemical energy applications.<sup>18,19</sup>

In this study, we report highly conductive off-stoichiometric  $\text{ZrO}_{2-x}$  nanofiber (NF) materials and their functionality as

catalytic electrode materials with enhanced electronic conductivities and surface activities. The electronic properties were successfully tuned by varying the reducing power in the thermal treatment of the  $\text{ZrO}_{2-x}$  NFs. By simultaneously generating  $\text{Zr}^{3+}$  and oxygen vacancies in the  $\text{ZrO}_{2-x}$  NFs, diverse  $\text{ZrO}_{2-x}$  NFs were obtained, with different colors, from white, to brown, to black, reflecting the tunable optical properties. The structural and morphological characteristics of the  $\text{ZrO}_{2-x}$  NFs are investigated in detail using various material characterization techniques. We measured bandgap properties related to the conductivities and accordingly elucidated the enhanced catalytic activities of the black  $\text{ZrO}_{2-x}$  NFs. This study paves the way for the development of multifunctional valve metal oxides simultaneously exhibiting high conductivities and improved catalytic activities in addition to their structural stabilities.

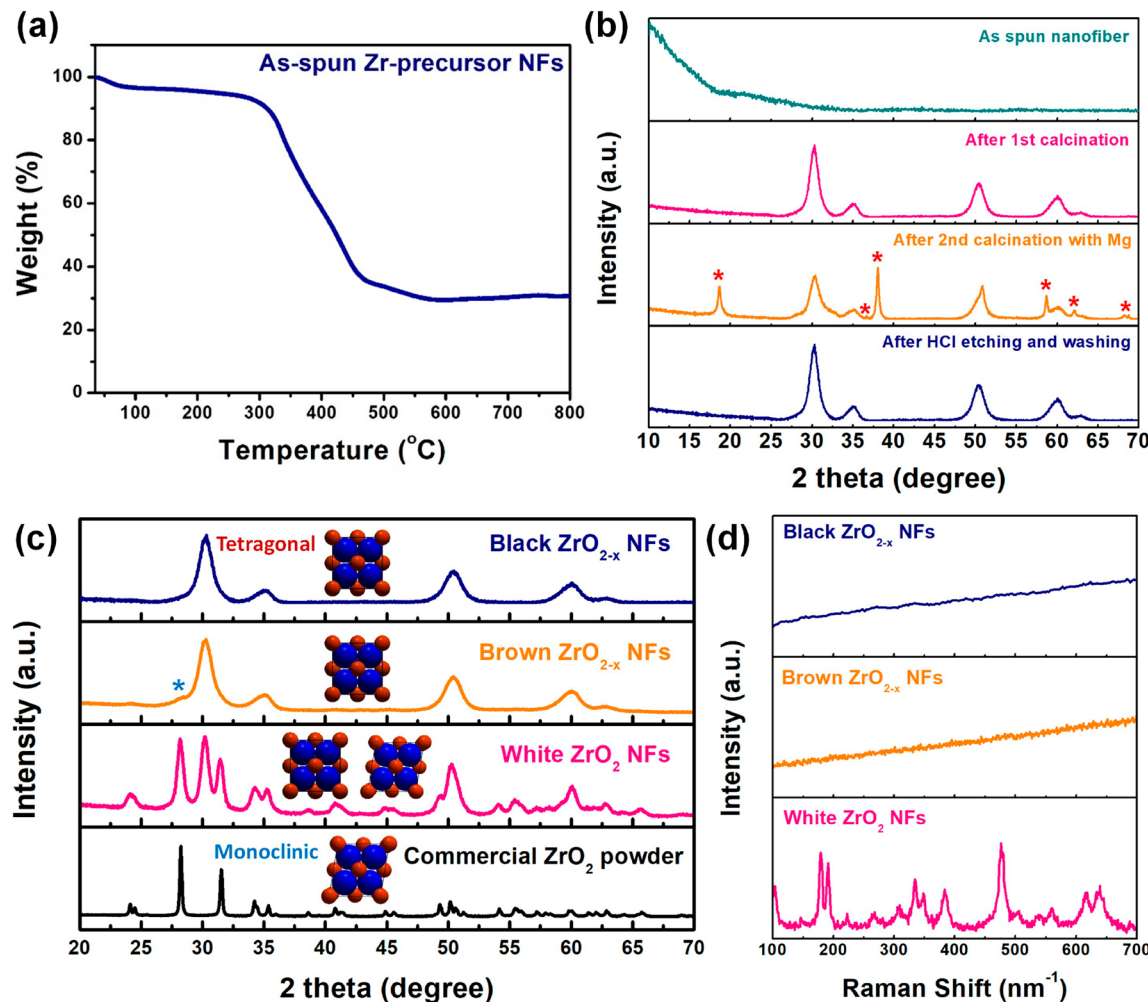


**Figure 2.** (a) TGA curve of the as-spun composite NFs of Zr precursor with the PVP polymer as a function of the temperature in air. (b) XRD patterns of the as-spun NFs, NFs after the first calcination, NFs after the second calcination with Mg, and NFs after the second calcination, etching, and washing. (c) XRD patterns of the commercial  $ZrO_2$  powder and white  $ZrO_2$ , brown  $ZrO_{2-x}$ , and black  $ZrO_{2-x}$  NFs. The insets in panel c are top-view ( $x-z$  plane) schematics of corresponding unit cells of the monoclinic and tetragonal  $ZrO_2$ . The blue asterisk (\*) indicates the monoclinic phase. (d) Raman spectra of the white  $ZrO_2$ , brown  $ZrO_{2-x}$ , and black  $ZrO_{2-x}$  NFs.

## RESULTS AND DISCUSSION

In order to synthesize the black  $ZrO_{2-x}$  nanostructure, we used the electrospinning method, which is a versatile and simple approach to form one-dimensional and continuous NFs with diverse atomic compositions (Figure 1a).<sup>20–22</sup> A two-step thermal treatment of the as-spun Zr-precursor/poly(vinylpyrrolidine) (PVP) composite NFs is carried out. The first calcination at a low temperature of 350 °C in air was performed to decompose the polymer template in the NF and form a  $ZrO_2$  phase. The oxidation state of Zr and resultant oxygen stoichiometry were controlled by a subsequent thermal treatment under a different atmosphere. Unlike the white  $ZrO_2$  phase prepared under air, brown and black  $ZrO_{2-x}$  NFs were obtained by calcination under a reducing atmosphere ( $H_2/Ar$ ). In the case of black  $ZrO_{2-x}$ , Mg powder, known as a strong reducer, is additionally mixed with preheated  $ZrO_2$  NFs, which are calcined together under the reductive  $H_2/Ar$  atmosphere.<sup>23,24</sup> We successfully prepared different  $ZrO_2$  or  $ZrO_{2-x}$  NFs with diverse optical colors (white, brown, and black) (Figure 1b), which correspond to different bandgaps and electronic conductivities. The morphologies of the as-spun fibers were uniform and continuous with diameters of 300 nm

(Figure 1c,d). After the first thermal treatment, the fibers shrank to diameters of approximately 190 nm owing to the thermal decomposition of the PVP polymer and precursor species (Figure 1e). Even after the subsequent calcination under a different atmosphere, the fiber shape and diameter did not change, which implies that analogous morphological effects can be considered among all of the NF samples (Figure 1f–h and Supporting Information Figure S1).

We investigated the thermal decomposition behaviors of the as-spun Zr-precursor NFs using a thermogravimetric analysis (TGA) under air (Figure 2a). The slight decrease in weight at 100 °C is related to the evaporation of residual water in the precursor NFs. A sudden weight loss is observed after 300 °C due to the decomposition of the PVP polymer and precursor species (i.e., acetates).<sup>14</sup> Based on the TGA results, we chose 350 °C as the temperature for the first thermal treatment. The extensive decomposition of the PVP polymer decreased the fiber diameter (300 nm → 190 nm), as shown in the scanning electron microscopy (SEM) image of the NFs obtained after the first calcination (Figure 1e). The relatively low temperature of 350 °C for the thermal pretreatment can provide structural relaxation of the low-crystallinity  $ZrO_2$  phase and its facile

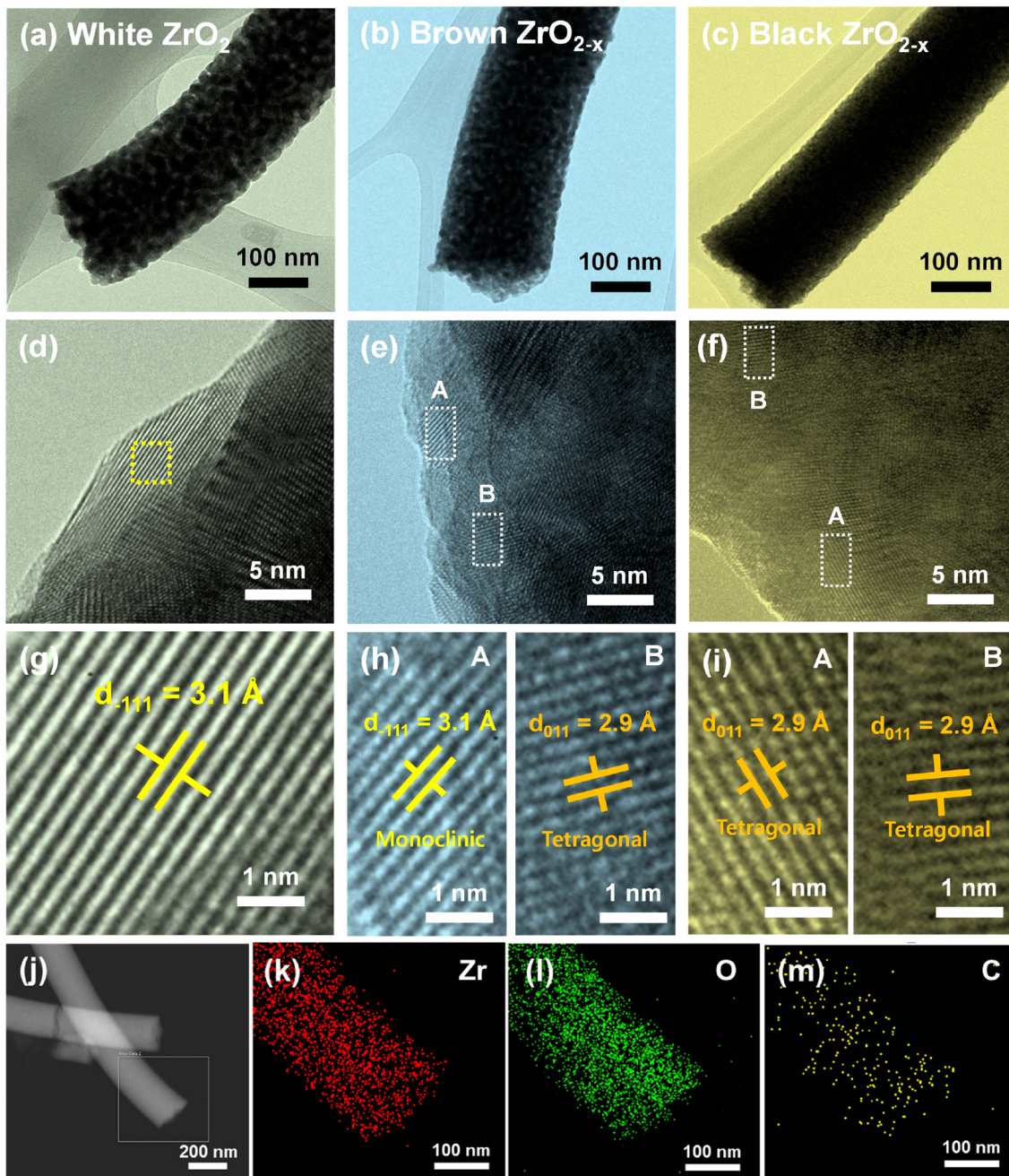


**Figure 3.** TEM images of the (a) white  $\text{ZrO}_2$ , (b) brown  $\text{ZrO}_{2-x}$  and (c) black  $\text{ZrO}_{2-x}$  NFs. Magnified TEM images of the (d) white  $\text{ZrO}_2$ , (e) brown  $\text{ZrO}_{2-x}$  and (f) black  $\text{ZrO}_{2-x}$  NFs. Lattice fringes of the (g) white  $\text{ZrO}_2$ , (h) brown  $\text{ZrO}_{2-x}$  and (i) black  $\text{ZrO}_{2-x}$  NFs observed in the corresponding regions in panels d–f, respectively. (j) STEM image of the black  $\text{ZrO}_{2-x}$  NFs and element maps of (k) Zr, (l) O, and (m) C, acquired from the selected area in panel j.

conversion to diverse  $\text{ZrO}_{2-x}$  phases at the thermal post-treatment at 600 °C. Carbon residues converted from the polymer template are fully removed after the thermal post-treatment. X-ray diffraction (XRD) analysis of the NFs was carried out to investigate crystalline features of the NFs obtained at each intermediate stage (Figure 2b). The as-spun fibers composed of Zr precursor and PVP polymer are amorphous. The tetragonal  $\text{ZrO}_2$  phase (Joint Committee on Powder Diffraction Standards (JCPDS) No. 50-1089) is formed by the first calcination in air, consistent with the TGA results. We performed the second thermal treatment in an oxidative or reductive environment to obtain white  $\text{ZrO}_2$  or

brown  $\text{ZrO}_{2-x}$  NFs, respectively. In order to provide a stronger reducing environment for the formation of the black  $\text{ZrO}_{2-x}$  phase, we mixed Mg powder with the  $\text{ZrO}_2$  NFs obtained from the first calcination. The Mg powder tends to oxidize by oxygen species from the  $\text{ZrO}_2$  NFs, thus transforming to the  $\text{MgO}$  phase. The  $\text{MgO}$  powder is easily removed by HCl etching and subsequent washing treatment. We observed the XRD peaks corresponding to the tetragonal  $\text{ZrO}_{2-x}$  and  $\text{MgO}$  phases after the second calcination (Figure 2b). The results demonstrate that the Mg powder effectively acts as a reducing agent and consequently transforms into the  $\text{MgO}$  phase. After the etching in HCl and following a washing process, a

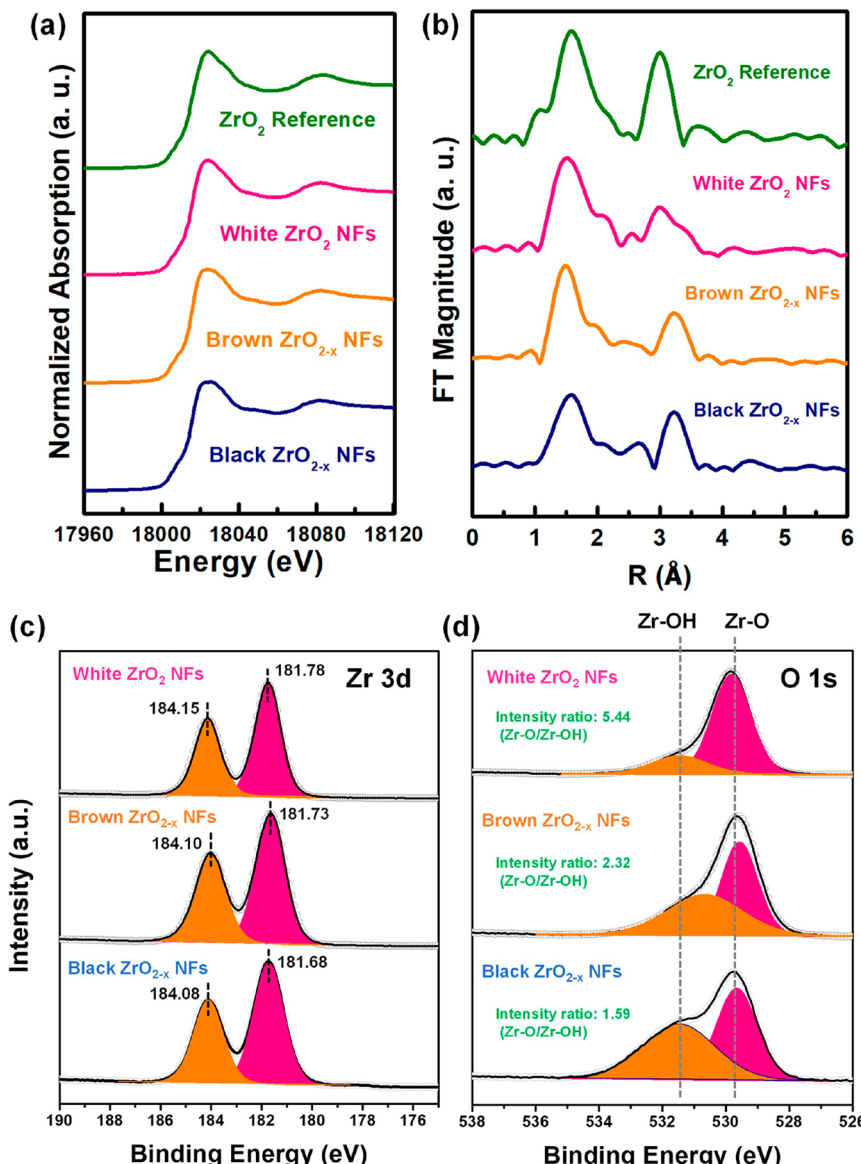


**Figure 4.** (a) Normalized Zr K-edge XANES spectra and (b) corresponding  $k^3$ -weighted Fourier transforms (FTs) of the commercial  $\text{ZrO}_2$  reference and white  $\text{ZrO}_2$ , brown  $\text{ZrO}_{2-x}$ , and black  $\text{ZrO}_{2-x}$  NFs. XPS of the white  $\text{ZrO}_2$ , brown  $\text{ZrO}_{2-x}$ , and black  $\text{ZrO}_{2-x}$  NFs for (c) Zr 3d and (d) O 1s.

negligible  $\text{MgO}$  residue exists in the product sample, while the tetragonal  $\text{ZrO}_{2-x}$  structure is maintained without any damage. We investigated the crystalline phase structures of the various  $\text{ZrO}_{2-x}$  NFs with diverse optical colors (Figure 2c). The commercial  $\text{ZrO}_2$  powder is purely monoclinic (JCPDS No. 65o1023), while the white  $\text{ZrO}_2$  NFs exhibit a mixed phase of monoclinic and tetragonal structures. With the increase in the reducing power in the synthesis, the monoclinic feature is diminished and the tetragonal phase becomes dominant. The shoulder peak of the monoclinic phase at  $28.2^\circ$  (in the figure, blue asterisk (\*) for the brown  $\text{ZrO}_{2-x}$  NFs) is not observed for the black  $\text{ZrO}_{2-x}$  NF sample. The formation of oxygen defect sites in the structure could distort the  $\text{ZrO}_{2-x}$  lattice. The black  $\text{ZrO}_{2-x}$  NFs exhibit only the tetragonal structure instead of the monoclinic structure. The tetragonal phase could be dominantly located inside the white NFs, while the monoclinic structure can be preferentially formed on the surface under the oxidative calcination. Raman spectroscopy was employed to investigate the Zr–O vibration mode, which

is associated with the surface and lattice disorders in the first atomic shells (Figure 2d). The white  $\text{ZrO}_2$  NFs exhibit the O–Zr–O vibration mode in the  $\text{ZrO}_2$  lattice, while no significant peaks are observed in the Raman spectra of both brown and black  $\text{ZrO}_{2-x}$  NFs owing to peak broadening. These results are attributed to localized defects (e.g., oxygen vacancies) in the lattice, indicating the formation of the nonstoichiometric  $\text{ZrO}_{2-x}$  structure.<sup>14,17</sup>

The morphological shape and crystalline structures of the  $\text{ZrO}_{2-x}$  NFs were analyzed by transmission electron microscopy (TEM) (Figure 3 and Figure S2). The size of an individual crystallite particle in the brown and black  $\text{ZrO}_{2-x}$  NF samples ( $\sim 5$  nm) is smaller than that of white  $\text{ZrO}_2$  NF ( $\sim 17$  nm) because growth of an individual particle to larger size is inhibited under reducing atmosphere during thermal treatment. Nevertheless, all of the NFs had almost equal diameters of approximately 200 nm, as shown by the SEM results (Figure 1e), which verifies that the surface area effect is insignificant among the samples (Figures 3a–c). Clear lattice fringes are

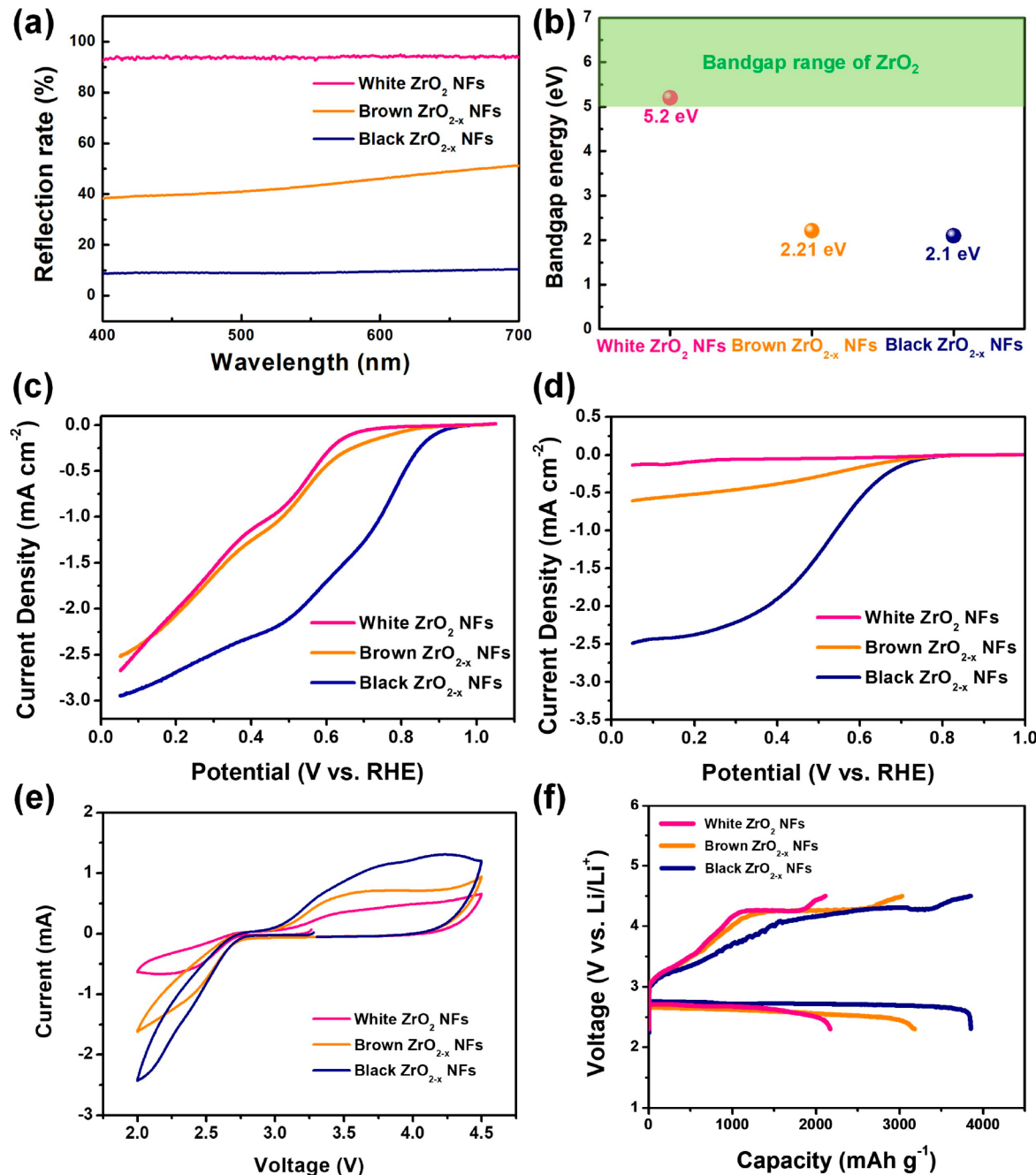


**Figure 5.** (a) Reflection rate curves and (b) calculated bandgaps of the white  $\text{ZrO}_2$ , brown  $\text{ZrO}_{2-x}$ , and black  $\text{ZrO}_{2-x}$  NFs. ORR polarization curves of the white  $\text{ZrO}_2$ , brown  $\text{ZrO}_{2-x}$ , and black  $\text{ZrO}_{2-x}$  NFs in the  $\text{O}_2$ -saturated 0.1 M (c) KOH and (d)  $\text{HClO}_4$  solutions, obtained using a rotating disk electrode with a rotating speed of 1600 rpm. The electrochemical tests are performed without carbon supports to exactly evaluate their oxygen reduction activities. (e) CV curves of the Li-O<sub>2</sub> cells with the white  $\text{ZrO}_2$ , brown  $\text{ZrO}_{2-x}$ , and black  $\text{ZrO}_{2-x}$  NFs in the electrolyte of 1 M LiTFSI + DEGDME after the  $\text{O}_2$  purging. (f) Initial charge/discharge curves of the Li-O<sub>2</sub> cells with the white  $\text{ZrO}_2$ , brown  $\text{ZrO}_{2-x}$ , and black  $\text{ZrO}_{2-x}$  NFs at a current density of 100 mA g<sup>-1</sup> carbon.

observed in the magnified images of all of the samples; this is attributed to the high crystallinities of the NFs (Figure 3d–f). The monoclinic phase disappeared from the mixed phase (monoclinic and tetragonal) in the XRD results of the  $\text{ZrO}_{2-x}$  NFs synthesized under the severe reducing atmosphere (Figure 2c). The dominant lattice spacing of the monoclinic structure is observed for the white  $\text{ZrO}_2$  NFs ( $d_{\bar{1}11} = 3.1 \text{ \AA}$ ) (Figure 3g). On the other hand, local tetragonal phases ( $d_{011} = 2.9 \text{ \AA}$ ) and monoclinic phases coexist in the brown  $\text{ZrO}_{2-x}$  NFs (Figure 3h). Further, no significant monoclinic region is observed in

the black  $\text{ZrO}_{2-x}$  NFs, which indicates the phase conversion of the monoclinic to the tetragonal structure during the calcination under the reducing environment, consistent with the XRD results (Figures 3i and 2c). In order to investigate the atomic distribution in the black  $\text{ZrO}_{2-x}$  NFs, we employed scanning transmission electron microscopy–energy-dispersive spectroscopy (STEM–EDS) elemental mapping (Figure 3j–m). The Zr and O species were uniformly distributed throughout the fibers. In contrast, low C contents exist in the samples. The elemental analysis in Table S1 confirms the

negligible carbon contents of 0.44 and 1.4 wt % in the brown and black  $\text{ZrO}_{2-x}$  NFs, respectively, demonstrating that the different optical colors of the samples originated from the change in bandgap of  $\text{ZrO}_{2-x}$  rather than from the presence of carbon.

The local structures around Zr atoms in the  $\text{ZrO}_2$  samples were analyzed through X-ray absorption spectroscopy (XAS) to fully resolve the atomic structures of the samples (Figure 4a,b). Both X-ray absorption near-edge structure (XANES) and extended X-ray absorption fine structure (EXAFS) analyses confirmed that a phase transformation occurred from the monoclinic to the tetragonal structure, as revealed in the XRD observations. In contrast to the brown and black  $\text{ZrO}_{2-x}$  NF samples, the XANES spectra of the  $\text{ZrO}_2$  reference and white  $\text{ZrO}_2$  NFs show sharp white-line peaks near 18,024 eV, which indicate that the  $\text{ZrO}_2$  reference and white  $\text{ZrO}_2$  NFs have typical monoclinic structures (Figure 4a).<sup>25</sup> The shape evolution of the white line from sharp ( $\text{ZrO}_2$  reference and white  $\text{ZrO}_2$  NFs) to broad (brown and black  $\text{ZrO}_{2-x}$  NFs) in the XANES spectra is mainly caused by the different symmetric Zr–O coordination (Figure 4a and Figure S3).<sup>25,26</sup> The pre-edge peak around 18,026 eV also indicates the phase change from the monoclinic to the tetragonal  $\text{ZrO}_2$ . The tetragonal  $\text{ZrO}_2$  exhibits a prominent pre-edge peak in the XANES spectrum owing to the  $1s \rightarrow 4d$  transition attributed to some p–d mixing.<sup>26</sup> As the Zr–O geometry of the tetragonal  $\text{ZrO}_2$  enhances the p–d mixing and distorted centrosymmetry of the tetragonal  $\text{ZrO}_2$  from the non-equivalent tetrahedral, the intensities of these transition peaks of the brown and black  $\text{ZrO}_{2-x}$  NF samples are higher than that of the  $\text{ZrO}_2$  reference.<sup>27</sup> Additionally, the shoulder peak near 18,050 eV of the black  $\text{ZrO}_{2-x}$  NFs originated from multiple scatterings due to second-nearest-neighbor atoms or higher shells, particularly in the tetragonal structure.<sup>25</sup> In addition to the XANES analysis, an EXAFS analysis is performed, which shows the phase transitions of the samples from the monoclinic to the tetragonal structures by determining interatomic distances. The first peak near 1.5 Å in the EXAFS spectra (Figure 4b) is attributed to the Zr–O pair, while the second main peak around 3 Å is attributed to the Zr–Zr pair.<sup>26</sup> The changes in the shape and peak position of the second peak (Zr–Zr) in our samples are more prominent than those of the first peak (Zr–O). The second peaks of the  $\text{ZrO}_2$  reference and white  $\text{ZrO}_2$  NF samples are located at 3 Å, while for the brown and black  $\text{ZrO}_{2-x}$  NF samples, they appear around 3.3 Å. This peak shift, from 3 to 3.3 Å, shows that there are two distinct structures, monoclinic and tetragonal, respectively.<sup>25,26</sup> The analysis of the XANES and EXAFS spectra verifies that the  $\text{ZrO}_2$  reference has the monoclinic structure while the black  $\text{ZrO}_{2-x}$  NF sample has the tetragonal structure. The dominant crystal structures of the white  $\text{ZrO}_2$  and brown  $\text{ZrO}_{2-x}$  NFs are monoclinic and tetragonal, respectively. As XAS is a bulk characterization as well as amorphous-sensitive technique, the results present all of the phase transformations of entire samples.

A surface characterization of the nonstoichiometric  $\text{ZrO}_{2-x}$  NFs obtained under the different reducing atmospheres is carried out to further evaluate the oxidation state of Zr and resulting oxygen defects (Figure 4c,d). The Zr 3d core-level X-ray photoelectron spectra (XPS) of the white, brown, and black  $\text{ZrO}_{2-x}$  NFs had two distinct peaks corresponding to the characteristic Zr 3d<sub>3/2</sub> and Zr 3d<sub>5/2</sub> peaks (Figure 4c).<sup>28</sup> For the white  $\text{ZrO}_2$  NFs, the Zr 3d<sub>3/2</sub> and Zr 3d<sub>5/2</sub> peaks were

centered at  $\sim$ 184.15 and  $\sim$ 181.78 eV, respectively, which were related to  $\text{Zr}^{4+}$  in  $\text{ZrO}_2$ .<sup>29</sup> On the other hand, relative shifts of these two peaks to lower binding energies were observed for the brown and black  $\text{ZrO}_{2-x}$  NFs, demonstrating the transformation of the Zr–O bonding structure. It has been reported that the shifted peaks corresponded to the Zr 3d<sub>3/2</sub> and Zr 3d<sub>5/2</sub> peaks of  $\text{Zr}^{3+}$ , which verified the room-temperature-stable isolated  $\text{Zr}^{3+}$  defect structure in the  $\text{ZrO}_{2-x}$  NFs.<sup>12,30</sup>  $\text{Zr}^{3+}$  and oxygen vacancies were simultaneously generated in the reductive calcination of  $\text{ZrO}_2$  to satisfy the charge neutrality. The high oxygen deficiencies in  $\text{ZrO}_{2-x}$  originated either from the oxygen release from the anion sublattice or from the formation of Zr interstitials. The oxygen defect sites in the negative-type (n-type)  $\text{ZrO}_{2-x}$ , known as electron donor, can facilitate the movement of charges (mainly electrons). The O 1s core-level XPS analyses of the NF samples are presented in Figure 4d. All of the samples exhibit two peaks, at  $\sim$ 531.8 and  $\sim$ 529.8 eV, corresponding to the characteristic peaks of Zr–OH and Zr–O, respectively.<sup>29</sup> The intensity of the Zr–OH peak is further increased for the  $\text{ZrO}_{2-x}$  NF samples obtained under the reductive atmosphere. The intensity ratios (Zr–O/Zr–OH) for the white  $\text{ZrO}_2$ , brown  $\text{ZrO}_{2-x}$ , and black  $\text{ZrO}_{2-x}$  NFs were 5.44, 2.32, and 1.59, respectively. Oxygen defects in  $\text{ZrO}_{2-x}$  can easily bind with hydrogen atoms and subsequently form hydroxyl groups on the surface. This clearly supports the results that nonstoichiometric  $\text{ZrO}_{2-x}$  NFs with different amounts of  $\text{Zr}^{3+}$  and oxygen vacancies were successfully fabricated.

The higher donor density in the  $\text{ZrO}_{2-x}$  structure increases the electrical conductivity owing to the decrease in the bandgap. In order to determine the improved electrical conductivities of the brown and black  $\text{ZrO}_{2-x}$  NFs, we analyzed the reflectance rates and calculated the bandgaps of the NF samples using the Tauc equation (Figures 5a,b and S4).<sup>31,32</sup> A high reflectance rate (low absorption) of  $\sim$ 94% and bandgap of 5.2 eV are obtained for the white  $\text{ZrO}_2$  NFs (Figure 5a). Typical  $\text{ZrO}_2$  materials, close to insulator, exhibit bandgaps in a broad range of 5–7 eV (Figure 5b).<sup>33</sup> In contrast, lower reflectance rates (higher absorption) of  $\sim$ 39% and  $\sim$ 9% are estimated for the brown and black  $\text{ZrO}_{2-x}$  NFs, corresponding to lower bandgaps of 2.21 and 2.1 eV, respectively. Considering the negligible carbon contents (approximately 1 wt %) in the brown and black  $\text{ZrO}_{2-x}$  NFs, the low bandgaps of approximately  $\sim$ 2 eV reflect the formation of the  $\text{ZrO}_{2-x}$  phase owing to the reduction of  $\text{Zr}^{4+}$  to  $\text{Zr}^{3+}$ . The decreased bandgap, originated from the existence of  $\text{Zr}^{3+}$  and oxygen vacancies, leads to a fast transport of charge carriers (electron and ions) in the NFs. In addition, the oxygen defects can act as effective absorption and catalytic reaction sites for oxygen reduction reaction (ORR) and oxygen evolution reaction (OER).<sup>34–37</sup> The electrochemical catalytic activity was evaluated by ORR and OER tests in acid and alkaline solutions (Figure 5c,d).<sup>38</sup> Although the ORR current density values are very low ( $-2.5$  to  $-3.0 \text{ mA cm}^{-2}$ ) owing to the intrinsically low electrical conductivity of  $\text{ZrO}_2$ , the black  $\text{ZrO}_{2-x}$  NFs exhibited the highest ORR performance with an onset potential of 0.959 V followed by the white  $\text{ZrO}_2$  ( $E_{\text{onset}} = 0.914$  V) and brown  $\text{ZrO}_{2-x}$  ( $E_{\text{onset}} = 0.838$  V) NFs in a 0.1 M KOH solution. The white  $\text{ZrO}_2$  NFs exhibited an almost negligible ORR activity in a 0.1 M  $\text{HClO}_4$  solution, as the typical  $\text{ZrO}_2$  is insulator and catalytically inactive (Figure 5c). In contrast, gradual increases in cathodic current densities were

observed for the brown and black  $\text{ZrO}_{2-x}$  NFs with positive shifts of the onset potentials (0.845 and 0.856 V for the brown and black  $\text{ZrO}_{2-x}$ , respectively). This implies that the partial deficiency of oxygen in the  $\text{ZrO}_2$  lattice structure can provide enhanced ORR activities and electrical conductivities. Figure S5 compares the ORR catalytic activities of the black  $\text{ZrO}_{2-x}$  NFs in the alkaline and acid media. The ORR activity of the black  $\text{ZrO}_{2-x}$  NFs in the alkaline solution is significantly higher than that in the acidic solution. The half-wave potential ( $E_{1/2}$ ) is positively shifted by 144.6 mV, from 509.1 mV in the 0.1 M  $\text{HClO}_4$  solution to 653.7 mV in the 0.1 M KOH solution. The Tafel slopes of the black  $\text{ZrO}_{2-x}$  NFs are 85 and 113 mV dec<sup>-1</sup> in the 0.1 M KOH and  $\text{HClO}_4$  solutions, respectively. In order to demonstrate the robustness of the sample during the ORR, we carried out chronoamperometric tests at a fixed potential of 0.6 V in alkaline media. Compared to the commercial Pt/C, known as the best ORR catalyst, a better stability with a smaller decrease in current density (~75.5%) for 12,000 s was observed for the black  $\text{ZrO}_{2-x}$  NFs (Figure S6). The commercial Pt/C exhibited a gradual loss of its initial current (~65.3%) during the 12,000 s. The distinct stability of the black  $\text{ZrO}_{2-x}$  NFs under the applied reductive potential in the alkaline medium suggests the possibility to use the  $\text{ZrO}_{2-x}$  NFs as support materials or functional scaffold for an ORR catalyst (i.e., Pt or Au in proton-exchange membrane fuel cells (PEMFCs)).<sup>39</sup> On the other hand, all of the NFs exhibited negligible differences in the OER activities in the alkaline solution (Figure S7).

We compared the electrochemical properties of the  $\text{ZrO}_{2-x}$  NFs as oxygen electrode catalysts in a nonaqueous lithium oxygen ( $\text{Li}-\text{O}_2$ ) cell to demonstrate their bifunctional advantages in different catalytic systems. The  $\text{Li}-\text{O}_2$  cell operates through oxygen reduction and evolution for discharging and charging on the electrode surface, respectively ( $2\text{Li}^+ + \text{O}_2 + 2\text{e}^- \leftrightarrow 2\text{Li}_2\text{O}_2$ ,  $E^\circ = 2.96$  V vs Li/Li<sup>+</sup>).<sup>40,41</sup> The electrochemical activity in the nonaqueous electrolyte in a wide voltage range around 4 V exhibits a unique behavior compared to that in an aqueous electrolyte at 1 V. The  $\text{Li}-\text{O}_2$  cell reaction occurs based on a gas-to-solid reaction, in contrast to the gas-to-liquid reaction ( $4\text{H}^+ + \text{O}_2 + 4\text{e}^- \leftrightarrow 2\text{H}_2\text{O}$ ,  $E^\circ = 0$  V vs H<sup>+</sup>/H<sub>2</sub>) in a fuel cell. Solid lithium oxide products are formed on the oxygen electrode surface for oxygen reduction (discharging), which are reversely decomposed for oxygen evolution (charging) in the  $\text{Li}-\text{O}_2$  cell.<sup>42,43</sup> However, the  $\text{Li}-\text{O}_2$  cell often suffers from a large ohmic resistance and resulting cell degradation due to the low electronic conductivities of the lithium oxide products.<sup>44</sup> Many studies have involved efficient catalysts on the electrode to facilitate the oxygen evolution reaction and improve the cell kinetics.<sup>45–50</sup> In order to analyze the catalytic activities of the  $\text{ZrO}_{2-x}$  NFs, cyclic voltammetry (CV) tests of the samples were carried out in a solution of 1 M lithium bis(trifluoromethanesulfonyl)imide (LiTFSI) in diethylene glycol dimethyl ether (DEGDME) (Figure 5e and Figure S8). All of the NF electrodes exhibit similar sloping curves in the cathodic region until 2.0 V and broad peaks in the anodic region until 4.5 V, related to the formation and reversible decomposition of lithium oxide products (i.e.,  $\text{LiO}_2$  and  $\text{Li}_2\text{O}_2$ ), respectively.<sup>47</sup> The current densities of the oxygen-deficient brown and black  $\text{ZrO}_{2-x}$  NFs in both cathodic and anodic regions are higher than those of the white  $\text{ZrO}_2$  NFs. The black  $\text{ZrO}_{2-x}$  NFs, which were prepared under a higher reducing power than that of the brown  $\text{ZrO}_{2-x}$  NFs, exhibit the highest current density among the samples. It is worth noting

that additional shoulder peaks were observed for the brown and black  $\text{ZrO}_{2-x}$  NFs, suggesting the catalytic activity in terms of formation of an intermediate superoxide ( $\text{O}_2^-$ ).<sup>46</sup> For the black  $\text{ZrO}_{2-x}$  NFs, a broad peak between two peaks near 3.2 and 4.1 V was observed in the anodic region, corresponding to the OER catalytic behavior. It is worth noting that no OER catalytic effect of the  $\text{ZrO}_{2-x}$  NFs was observed in the aqueous system, while enhanced OER activities were observed in the nonaqueous  $\text{Li}-\text{O}_2$  cell system. Further, we demonstrate the improved electrochemical performance of the  $\text{Li}-\text{O}_2$  cell with the black  $\text{ZrO}_{2-x}$  NF catalyst in an oxygen electrode, compared to that of the reference sample (Figure 5f). The  $\text{Li}-\text{O}_2$  cell with black  $\text{ZrO}_{2-x}$  NFs exhibits higher discharge capacity (3,850 mAh g<sup>-1</sup>) and Coulombic efficiency (almost 100%) than those of the white  $\text{ZrO}_2$  (2,168 mAh g<sup>-1</sup>, 96%) and brown  $\text{ZrO}_{2-x}$  (3,175 mAh g<sup>-1</sup>, 96.5%) NFs, which are consistent with the CV results. Therefore, the  $\text{Li}-\text{O}_2$  cell reaction can be facilitated by the introduction of the black  $\text{ZrO}_{2-x}$  NFs. White  $\text{ZrO}_2$  NFs are rarely considered a component of an electrode except for mechanically or chemically resistive purposes owing to its low charge conductivities for both electrons and ions. Our findings show that black  $\text{ZrO}_{2-x}$  NFs could be utilized as an efficient and robust catalyst material in electrodes for future energy applications.

## CONCLUSION

In summary, we fabricated highly conductive off-stoichiometric  $\text{ZrO}_{2-x}$  NF materials with controllable electronic and optical properties and analyzed their potentials as catalytic electrode components for energy applications. We successfully synthesized the  $\text{ZrO}_{2-x}$  NFs by electrospinning of Zr-precursor composite fibers and subsequent two-step calcination in air and reducing atmosphere. We finely controlled the degree of oxygen deficiency and resultant bandgap properties of the  $\text{ZrO}_{2-x}$  NFs by varying the reducing power in the second calcination. The morphological and structural features of the  $\text{ZrO}_{2-x}$  NF materials obtained under the different reducing atmospheres were investigated. The tetragonal phase became dominant, instead of the mixed phase of tetragonal and monoclinic structures, upon the increase in the number of oxygen defects in the  $\text{ZrO}_{2-x}$  NFs. The oxygen defects and tuned Zr oxidation states in the  $\text{ZrO}_{2-x}$  NFs were confirmed by surface characterizations. The improved charge transport in the  $\text{ZrO}_{2-x}$  NFs owing to the reduced bandgap could facilitate the electrochemical reactions in both aqueous and nonaqueous systems. We also confirmed enhanced stability of the  $\text{ZrO}_{2-x}$  NFs as a functional scaffold for an ORR catalyst. The fine structural engineering of the valve metal oxide could provide a novel approach to develop alternative electrode materials for multifunctional devices with high durabilities and improved charge conductivities.

## ASSOCIATED CONTENT

### Supporting Information

The Supporting Information is available free of charge on the ACS Publications website at DOI: 10.1021/acsaelm.9b00283.

Experimental procedure, element analysis data, additional SEM images of nanofiber samples, normalized Zr K-edge XANES spectra, Tauc plots, additional electrochemical data (ORR polarization curves, Tafel plots,

chronoamperometric profiles, OER polarization curves, and CV curves) ([PDF](#))

## AUTHOR INFORMATION

### Corresponding Author

\*E-mail: [whryu@sookmyung.ac.kr](mailto:whryu@sookmyung.ac.kr).

### ORCID

Don-Hyung Ha: [0000-0003-4744-6571](#)

Won-Hee Ryu: [0000-0002-0203-2992](#)

### Notes

The authors declare no competing financial interest.

## ACKNOWLEDGMENTS

This work was supported by the National Research Foundation of Korea (NRF) grant funded by the Korea government (MSIT) (No. 2019R1C1C1007886). This research was also supported by the Korea Evaluation Institute of Industrial Technology (KEIT) grant funded by the Korea government (MOTIE) (No. 10077594). This work was supported by the National Research Foundation of Korea (NRF) grant funded by the Korea government (MSIT) (No. 2018R1A5A1025224).

## REFERENCES

- (1) Hunter, B. M.; Gray, H. B.; Müller, A. M. Earth-Abundant Heterogeneous Water Oxidation Catalysts. *Chem. Rev.* **2016**, *116*, 14120–14136.
- (2) Yuan, C.; Wu, H. B.; Xie, Y.; Lou, X. W. D. Mixed Transition-Metal Oxides: Design, Synthesis, and Energy-Related Applications. *Angew. Chem., Int. Ed.* **2014**, *53*, 1488–1504.
- (3) Robertson, J. Band offsets of wide-band-gap oxides and implications for future electronic devices. *J. Vac. Sci. Technol., B: Microelectron. Process. Phenom.* **2000**, *18*, 1785.
- (4) Hassel, A. W.; Diesing, D. Breakdown of ultrathin anodic valve metal oxide films in metal-insulator-metal-contacts compared with metal-insulator-electrolyte contacts. *Thin Solid Films* **2002**, *414*, 296–303.
- (5) Dignam, M. J. Conduction Properties of Valve Metal-Oxide Systems. *J. Electrochem. Soc.* **1965**, *112*, 729.
- (6) Nicholls, R. J.; Ni, N.; Lozano-Perez, S.; London, A.; McComb, D. W.; Nellist, P. D.; Grovenor, C. R. M.; Pickard, C. J.; Yates, J. R. Crystal Structure of the ZrO Phase at Zirconium/Zirconium Oxide Interfaces. *Adv. Eng. Mater.* **2015**, *17*, 211–215.
- (7) Manicone, P. F.; Rossi Iommelli, P.; Raffaelli, L. An overview of zirconia ceramics: Basic properties and clinical applications. *J. Dent.* **2007**, *35*, 819–826.
- (8) Gionco, C.; Livraghi, S.; Maurelli, S.; Giambello, E.; Tosoni, S.; Di Valentin, C.; Pacchioni, G. Al- and Ga-Doped TiO<sub>2</sub>, ZrO<sub>2</sub>, and HfO<sub>2</sub>: The Nature of O 2p Trapped Holes from a Combined Electron Paramagnetic Resonance (EPR) and Density Functional Theory (DFT) Study. *Chem. Mater.* **2015**, *27*, 3936–3945.
- (9) Chen, X.; Liu, L.; Yu, P. Y.; Mao, S. S. Increasing Solar Absorption for Photocatalysis with Black Hydrogenated Titanium Dioxide Nanocrystals. *Science* **2011**, *331*, 746–750.
- (10) Naldoni, A.; Allietti, M.; Santangelo, S.; Marelli, M.; Fabbri, F.; Cappelli, S.; Bianchi, C. L.; Psaro, R.; Dal Santo, V. Effect of Nature and Location of Defects on Bandgap Narrowing in Black TiO<sub>2</sub> Nanoparticles. *J. Am. Chem. Soc.* **2012**, *134*, 7600–7603.
- (11) Sani, E.; Mercatelli, L.; Sans, J.-L.; Sciti, D. Optical properties of black and white ZrO<sub>2</sub> for solar receiver applications. *Sol. Energy Mater. Sol. Cells* **2015**, *140*, 477–482.
- (12) Eom, J.-Y.; Lim, S.-J.; Lee, S.-M.; Ryu, W.-H.; Kwon, H.-S. Black titanium oxide nanoarray electrodes for high rate Li-ion microbatteries. *J. Mater. Chem. A* **2015**, *3*, 11183–11188.
- (13) Chen, X.; Liu, L.; Huang, F. Black titanium dioxide (TiO<sub>2</sub>) nanomaterials. *Chem. Soc. Rev.* **2015**, *44*, 1861–1885.
- (14) Lee, N.-W.; Jung, J.-W.; Lee, J.-S.; Jang, H.-Y.; Kim, I.-D.; Ryu, W.-H. Facile and fast Na-ion intercalation employing amorphous black TiO<sub>2</sub>-x/C composite nanofiber anodes. *Electrochim. Acta* **2018**, *263*, 417–425.
- (15) Liu, L.; Yu, P. Y.; Chen, X.; Mao, S. S.; Shen, D. Z. Hydrogenation and Disorder in Engineered Black TiO<sub>2</sub>. *Phys. Rev. Lett.* **2013**, *111*, 065505.
- (16) Ullatil, S. G.; Narendranath, S. B.; Pillai, S. C.; Periyat, P. Black TiO<sub>2</sub> Nanomaterials: A Review of Recent Advances. *Chem. Eng. J.* **2018**, *343*, 708–736.
- (17) Sinhamahapatra, A.; Jeon, J.-P.; Kang, J.; Han, B.; Yu, J.-S. Oxygen-Deficient Zirconia (ZrO<sub>2</sub>-x): A New Material for Solar Light Absorption. *Sci. Rep.* **2016**, *6*, 27218.
- (18) Li, W.; Huang, H.; Li, H.; Zhang, W.; Liu, H. Facile Synthesis of Pure Monoclinic and Tetragonal Zirconia Nanoparticles and Their Phase Effects on the Behavior of Supported Molybdena Catalysts for Methanol-Selective Oxidation. *Langmuir* **2008**, *24*, 8358–8366.
- (19) Pokrovski, K.; Jung, K. T.; Bell, A. T. Investigation of CO and CO<sub>2</sub> Adsorption on Tetragonal and Monoclinic Zirconia. *Langmuir* **2001**, *17*, 4297–4303.
- (20) Li, D.; Xia, Y. Electrospinning of Nanofibers: Reinventing the Wheel? *Adv. Mater.* **2004**, *16*, 1151–1170.
- (21) Wei, Q.; Xiong, F.; Tan, S.; Huang, L.; Lan, E. H.; Dunn, B.; Mai, L. Porous One-Dimensional Nanomaterials: Design, Fabrication and Applications in Electrochemical Energy Storage. *Adv. Mater.* **2017**, *29*, 1602300.
- (22) Ryu, W.-H.; Wilson, H.; Sohn, S.; Li, J.; Tong, X.; Shaulsky, E.; Schroers, J.; Elimelech, M.; Taylor, A. D. Heterogeneous WS<sub>x</sub>/WO<sub>3</sub> Thorn-Bush Nanofiber Electrodes for Sodium-Ion Batteries. *ACS Nano* **2016**, *10*, 3257–3266.
- (23) Bao, Z.; Weatherspoon, M. R.; Shian, S.; Cai, Y.; Graham, P. D.; Allan, S. M.; Ahmad, G.; Dickerson, M. B.; Church, B. C.; Kang, Z.; Abernathy, H. W., III; Summers, C. J.; Liu, M.; Sandhage, K. H. Chemical reduction of three-dimensional silica micro-assemblies into microporous silicon replicas. *Nature* **2007**, *446*, 172–175.
- (24) Ye, M.; Jia, J.; Wu, Z.; Qian, C.; Chen, R.; O'Brien, P. G.; Sun, W.; Dong, Y.; Ozin, G. A. Synthesis of Black TiO<sub>x</sub>Nanoparticles by Mg Reduction of TiO<sub>2</sub>Nanocrystals and their Application for Solar Water Evaporation. *Adv. Energy Mater.* **2017**, *7*, 1601811.
- (25) Meneghetti, F.; Wendel, E.; Mascotto, S.; Smarsly, B. M.; Tondello, E.; Bertagnoli, H.; Gross, S. Combined use of XAFS, XRD and TEM to unravel the microstructural evolution of nanostructured ZrO<sub>2</sub>–SiO<sub>2</sub> binary oxides: from nanometres down to the molecular domain. *CrystEngComm* **2010**, *12*, 1639–1649.
- (26) Li, P.; Chen, I. W.; Penner-Hahn, J. E. X-ray-absorption studies of zirconia polymorphs. I. Characteristic local structures. *Phys. Rev. B: Condens. Matter Mater. Phys.* **1993**, *48*, 10063–10073.
- (27) Jung, H.; Paek, S.-M.; Yoon, J.-B.; Choy, J.-H. Zr K-edge XAS study on ZrO<sub>2</sub>-pillared aluminosilicate. *J. Porous Mater.* **2007**, *14*, 369–377.
- (28) Ji, S.; Chang, I.; Lee, Y. H.; Park, J.; Paek, J. Y.; Lee, M. H.; Cha, S. W. Fabrication of low-temperature solid oxide fuel cells with a nanothin protective layer by atomic layer deposition. *Nanoscale Res. Lett.* **2013**, *8*, 48.
- (29) Vempati, S.; Kayaci-Senirmak, F.; Ozgit-Akgun, C.; Biyikli, N.; Uyar, T. Amorphous to Tetragonal Zirconia Nanostructures and Evolution of Valence and Core Regions. *J. Phys. Chem. C* **2015**, *119*, 23268–23273.
- (30) Guittet, M. J.; Crocombette, J. P.; Gautier-Soyer, M. Bonding and XPS chemical shifts in ZrSiO<sub>4</sub>versus SiO<sub>2</sub>and ZrO<sub>2</sub>: Charge transfer and electrostatic effects. *Phys. Rev. B: Condens. Matter Mater. Phys.* **2001**, *63*, 125117.
- (31) Huxter, V. M.; Mirkovic, T.; Nair, P. S.; Scholes, G. D. Demonstration of Bulk Semiconductor Optical Properties in Processable Ag<sub>2</sub>S and EuS Nanocrystalline Systems. *Adv. Mater.* **2008**, *20*, 2439–2443.

- (32) Ravi, O.; Prasad, K.; Jain, R.; Venkataswamy, M.; Chaurasia, S.; Deva Prasad Raju, B. Lasing transition at 1.06  $\mu\text{m}$  emission in Nd<sup>3+</sup>-doped borate-based tellurium calcium zinc niobium oxide glasses for high-power solid-state lasers. *Luminescence*. **2017**, *32*, 688–694.
- (33) Espinoza-González, R.; Mosquera, E.; Moglia, I.; Villarroel, R.; Fuenzalida, V. M. Hydrothermal growth and characterization of zirconia nanostructures on non-stoichiometric zirconium oxide. *Ceram. Int.* **2014**, *40*, 15577–15584.
- (34) Li, J.; Zhou, H.; Zhuo, H.; Wei, Z.; Zhuang, G.; Zhong, X.; Deng, S.; Li, X.; Wang, J. Oxygen vacancies on TiO<sub>2</sub> promoted the activity and stability of supported Pd nanoparticles for the oxygen reduction reaction. *J. Mater. Chem. A* **2018**, *6*, 2264–2272.
- (35) Yu, A.; Lee, C.; Kim, M. H.; Lee, Y. Nanotubular Iridium–Cobalt Mixed Oxide Crystalline Architectures Inherited from Cobalt Oxide for Highly Efficient Oxygen Evolution Reaction Catalysis. *ACS Appl. Mater. Interfaces* **2017**, *9*, 35057–35066.
- (36) Yu, M.; Wang, Z.; Hou, C.; Wang, Z.; Liang, C.; Zhao, C.; Tong, Y.; Lu, X.; Yang, S. Nitrogen-Doped Co<sub>3</sub>O<sub>4</sub>Mesoporous Nanowire Arrays as an Additive-Free Air-Cathode for Flexible Solid-State Zinc-Air Batteries. *Adv. Mater.* **2017**, *29*, 1602868.
- (37) Zhang, Y.; Wu, C.; Jiang, H.; Lin, Y.; Liu, H.; He, Q.; Chen, S.; Duan, T.; Song, L. Atomic Iridium Incorporated in Cobalt Hydroxide for Efficient Oxygen Evolution Catalysis in Neutral Electrolyte. *Adv. Mater.* **2018**, *30*, 1707522.
- (38) Yoon, K. R.; Choi, J.; Cho, S.-H.; Jung, J.-W.; Kim, C.; Cheong, J. Y.; Kim, I.-D. Facile preparation of efficient electrocatalysts for oxygen reduction reaction: One-dimensional meso/macroporous cobalt and nitrogen Co-doped carbon nanofibers. *J. Power Sources* **2018**, *380*, 174–184.
- (39) Ryu, W.-H.; Lee, Y. W.; Nam, Y. S.; Youn, D.-Y.; Park, C. B.; Kim, I.-D. Crystalline IrO<sub>2</sub>-decorated TiO<sub>2</sub> nanofiber scaffolds for robust and sustainable solar water oxidation. *J. Mater. Chem. A* **2014**, *2*, 5610–5615.
- (40) Bruce, P. G.; Freunberger, S. A.; Hardwick, L. J.; Tarascon, J. M. Li-O<sub>2</sub> and Li-S batteries with high energy storage. *Nat. Mater.* **2012**, *11*, 19–29.
- (41) Gallagher, K. G.; Goebel, S.; Greszler, T.; Mathias, M.; Oelerich, W.; Eroglu, D.; Srinivasan, V. Quantifying the promise of lithium-air batteries for electric vehicles. *Energy Environ. Sci.* **2014**, *7*, 1555–1563.
- (42) Ryu, W. H.; Gittleson, F. S.; Li, J. Y.; Tong, X.; Taylor, A. D. A New Design Strategy for Observing Lithium Oxide Growth-Evolution Interactions Using Geometric Catalyst Positioning. *Nano Lett.* **2016**, *16*, 4799–4806.
- (43) Ryu, W. H.; Gittleson, F. S.; Schwab, M.; Goh, T.; Taylor, A. D. A Mesoporous Catalytic Membrane Architecture for Lithium-Oxygen Battery Systems. *Nano Lett.* **2015**, *15*, 434–441.
- (44) Yao, X. H.; Dong, Q.; Cheng, Q. M.; Wang, D. W. Why Do Lithium-Oxygen Batteries Fail: Parasitic Chemical Reactions and Their Synergistic Effect. *Angew. Chem., Int. Ed.* **2016**, *55*, 11344–11353.
- (45) Ryu, W.-H.; Yoon, T.-H.; Song, S. H.; Jeon, S.; Park, Y.-J.; Kim, I.-D. Bifunctional Composite Catalysts Using Co<sub>3</sub>O<sub>4</sub> Nanofibers Immobilized on Nonoxidized Graphene Nanoflakes for High-Capacity and Long-Cycle Li–O<sub>2</sub> Batteries. *Nano Lett.* **2013**, *13*, 4190–4197.
- (46) Ryu, W. H.; Gittleson, F. S.; Thomsen, J. M.; Li, J. Y.; Schwab, M. J.; Brudvig, G. W.; Taylor, A. D. Heme biomolecule as redox mediator and oxygen shuttle for efficient charging of lithium-oxygen batteries. *Nat. Commun.* **2016**, *7*, 12925.
- (47) Lee, J.-S.; Lee, C.; Lee, J.-Y.; Ryu, J.; Ryu, W.-H. Polyoxometalate as a Nature-Inspired Bifunctional Catalyst for Lithium–Oxygen Batteries. *ACS Catal.* **2018**, *8*, 7213–7221.
- (48) Park, J. B.; Lee, S. H.; Jung, H. G.; Aurbach, D.; Sun, Y. K. Redox Mediators for Li-O<sub>2</sub> Batteries: Status and Perspectives. *Adv. Mater.* **2018**, *30*, 1704162.
- (49) Yoon, K. R.; Kim, D. S.; Ryu, W. H.; Song, S. H.; Youn, D. Y.; Jung, J. W.; Jeon, S.; Park, Y. J.; Kim, I. D. Tailored Combination of Low Dimensional Catalysts for Efficient Oxygen Reduction and Evolution in Li-O<sub>2</sub> Batteries. *ChemSusChem* **2016**, *9*, 2080–2088.
- (50) Lee, J.-S.; Kim, H.-S.; Ryu, W.-H. Iron/Carbon Composite Microfiber Catalyst Derived from Hemoglobin Blood Protein for Lithium-Oxygen Batteries. *Appl. Surf. Sci.* **2019**, *466*, 562–567.